

## Chemical compositions in the vicinity of protostars in Ophiuchus

KOTOMI TANIGUCHI,<sup>1</sup> LITON MAJUMDAR,<sup>2</sup> ADELE PLUNKETT,<sup>3</sup> SHIGEHISA TAKAKUWA,<sup>4</sup> DARIUSZ C. LIS,<sup>5</sup>  
PAUL F. GOLDSMITH,<sup>5</sup> FUMITAKA NAKAMURA,<sup>1,6,7</sup> MASAO SAITO,<sup>1,6</sup> AND ERIC HERBST<sup>8,9</sup>

<sup>1</sup>National Astronomical Observatory of Japan, National Institutes of Natural Sciences, 2-21-1 Osawa, Mitaka, Tokyo 181-8588, Japan

<sup>2</sup>School of Earth and Planetary Sciences, National Institute of Science Education and Research, HBNI, Jatni 752050, Odisha, India

<sup>3</sup>National Radio Astronomy Observatory, 520 Edgemont Rd., Charlottesville, VA 22903, USA

<sup>4</sup>Department of Physics and Astronomy, Graduate School of Science and Engineering, Kagoshima University, 1-21-35 Korimoto, Kagoshima, Kagoshima 890-0065, Japan

<sup>5</sup>Jet Propulsion Laboratory, California Institute of Technology, 48010 Oak Grove Drive, Pasadena, CA 91109, USA

<sup>6</sup>Department of Astronomical Science, School of Physical Science, SOKENDAI (The Graduate University for Advanced Studies), Osawa, Mitaka, Tokyo 181-8588, Japan

<sup>7</sup>The University of Tokyo, Hongo, Bunkyo, Tokyo 113-0033, Japan

<sup>8</sup>Department of Astronomy, University of Virginia, Charlottesville, VA 22904, USA

<sup>9</sup>Department of Chemistry, University of Virginia, Charlottesville, VA 22904, USA

Submitted to ApJ

### ABSTRACT

We have analyzed Atacama Large Millimeter/submillimeter Array (ALMA) Cycle 4 Band 6 data toward two young stellar objects (YSOs), Oph-emb5 and Oph-emb9, in the Ophiuchus star-forming region. The YSO Oph-emb5 is located in a relatively quiescent region, whereas Oph-emb9 is irradiated by a nearby bright Herbig Be star. Molecular lines from *cyclic*-C<sub>3</sub>H<sub>2</sub> (*c*-C<sub>3</sub>H<sub>2</sub>), H<sub>2</sub>CO, CH<sub>3</sub>OH, <sup>13</sup>CO, C<sup>18</sup>O, and DCO<sup>+</sup> have been detected from both sources, while DCN is detected only in Oph-emb9. Around Oph-emb5, *c*-C<sub>3</sub>H<sub>2</sub> is enhanced at the west side, relative to the IR source, whereas H<sub>2</sub>CO and CH<sub>3</sub>OH are abundant at the east side. In the field of Oph-emb9, moment 0 maps of the *c*-C<sub>3</sub>H<sub>2</sub> lines show a peak at the eastern edge of the field of view, which is irradiated by the Herbig Be star. Moment 0 maps of CH<sub>3</sub>OH and H<sub>2</sub>CO show peaks farther from the bright star. We derive the  $N(c\text{-C}_3\text{H}_2)/N(\text{CH}_3\text{OH})$  column density ratios at the peak positions of *c*-C<sub>3</sub>H<sub>2</sub> and CH<sub>3</sub>OH near each YSO, which are identified based on their moment 0 maps. The  $N(c\text{-C}_3\text{H}_2)/N(\text{CH}_3\text{OH})$  ratio at the *c*-C<sub>3</sub>H<sub>2</sub> peak is significantly higher than at the CH<sub>3</sub>OH peak by a factor of  $\sim 19$  in Oph-emb9, while the difference in this column density ratio between these two positions is a factor of  $\sim 2.6$  in Oph-emb5. These differences are attributed to the efficiency of the photon-dominated region (PDR) chemistry in Oph-emb9. The higher DCO<sup>+</sup> column density and the detection of DCN in Oph-emb9 are also discussed in the context of UV irradiation flux.

**Keywords:** astrochemistry — ISM: individual objects ( $\rho$  Oph A cloud,  $\rho$  Oph B cloud) — ISM: molecules — (ISM:) photon-dominated region (PDR)

### 1. INTRODUCTION

Chemical composition is a powerful tool with which to investigate the physical conditions and their evolution (Caselli & Ceccarelli 2012) from core scale ( $< 0.1$  pc)

to clump scale in molecular clouds ( $\sim 1$  pc; Taniguchi et al. 2020). These studies around low-mass protostars are essential for understanding the formation processes of our solar system and complex organic molecules detected in solar system bodies (Ceccarelli et al. 2017). Chemical differentiation around low-mass young stellar objects (YSOs) has been proposed since the late 2000s. One such chemical process is called hot-corino chemistry, which leads to abundant complex organic

molecules (COMs) consisting of more than six atoms (Herbst & van Dishoeck 2009). The other important one is called warm carbon-chain chemistry (WCCC; Sakai et al. 2008). Recent observations have shown chemical differentiation not only around low-mass YSOs, but around high-mass YSOs as well (Taniguchi et al. 2018, 2019b, 2021a). Although the origin of the chemical differentiation around YSOs is still controversial, three possible factors have been proposed: the different timescale of the prestellar collapse (Sakai et al. 2008), the different ultraviolet (UV) radiation field (Spezzano et al. 2016), and the different timescale of the warm-up stage (Taniguchi et al. 2019a). In order to reveal the effects of the above factors, we need to investigate molecular spatial distributions on large scales (e.g., the clump scale).

Our Sun is considered to have been born as a member of a cluster (Adams 2010; Jensen et al. 2019). In such a region, nearby sources may play important roles in chemical processes. One of the processes affecting chemical composition is UV radiation, as was suggested by Spezzano et al. (2016) based on observations toward starless cores. They found that CH<sub>3</sub>OH is abundant in a region well shielded against the interstellar radiation field, while *cyclic*-C<sub>3</sub>H<sub>2</sub> (hereafter *c*-C<sub>3</sub>H<sub>2</sub>) is enhanced in the irradiated environment. Such a chemical differentiation implies a different chemical composition in ice mantles, as shown by the CH<sub>4</sub>/CH<sub>3</sub>OH ice-mantle abundance ratio (Spezzano et al. 2016, 2020), because the gas-phase *c*-C<sub>3</sub>H<sub>2</sub> can be considered to form from CH<sub>4</sub> by the WCCC mechanism (Hassel et al. 2008). The UV radiation destroys CO molecules forming carbon atoms (C), which lead to the CH<sub>4</sub>-rich ice, and finally the carbon-chain-rich gas.

Chemical differentiation around low-mass YSOs has been studied using single-dish telescopes. Lindberg et al. (2016) carried out survey observations of C<sub>4</sub>H and CH<sub>3</sub>OH toward 16 low-mass YSOs in the Ophiuchus and Corona Australis molecular clouds using the Kitt Peak 12-m radio telescope and APEX. They proposed a spatial separation between these two types of molecules. Another study by Lindberg et al. (2017) presented APEX observations of H<sub>2</sub>CO and *c*-C<sub>3</sub>H<sub>2</sub> toward protostars in the Ophiuchus star-forming region. They suggested that the *c*-C<sub>3</sub>H<sub>2</sub> emission traces the more shielded parts of the envelope, whereas the H<sub>2</sub>CO emission mainly traces the outer irradiated envelopes. Their suggestion seems to be opposite to the finding in starless cores (Spezzano et al. 2016, 2020). Our target YSOs, identified as Oph-emb5 and Oph-emb9 in this paper, were also observed by Lindberg et al. (2016, 2017), and carbon-chain species (C<sub>4</sub>H and *c*-C<sub>3</sub>H<sub>2</sub>) and COMs (CH<sub>3</sub>OH and H<sub>2</sub>CO) have been detected from

both YSOs. These studies (Lindberg et al. 2016, 2017), however, were single-dish single-pointing observations, and spatial variation among these molecular lines were not resolved. High-angular resolution and high sensitivity observations are needed to study the effects of UV radiation on chemical composition around YSOs in order to distinguish between nearby sources and target YSOs.

In this paper, we report ALMA Band 6 data toward two YSOs in the Ophiuchus region. The Ophiuchus region is a nearby star-forming region ( $\sim 140$  pc Ortiz-León et al. 2018) with Class II YSOs relatively more abundant than YSOs of other classes, similar to the Lupus I region and the Chamaeleon region (Dunham et al. 2015). A bright Herbig Be star (S1) irradiates the  $\rho$  Oph A cloud (Lindberg et al. 2017). The YSO Oph-emb9, one of our target sources, is located in this cloud and is irradiated by the Herbig Be star from the east. The YSO Oph-emb5 is located in the  $\rho$  Oph B cloud with no nearby irradiation sources. The distance between the  $\rho$  Oph A cloud and the  $\rho$  Oph B cloud is around 0.55 pc, and we can assume that the other initial conditions are comparable. Thus, these are good target regions to study effects of nearby bright sources on the chemical differentiation around YSOs.

The structure of the present paper is as follows. In Section 2, we explain the data sets and reduction procedure. The resultant continuum maps are presented in Section 3.1, moment 0 maps of the detected molecular lines are shown in Section 3.2, spectra and spectral analyses are presented in Section 3.3, and finally moment 2 maps of <sup>13</sup>CO and C<sup>18</sup>O are shown in Section 3.4. Our main conclusions are summarized in Section 4.

## 2. OBSERVATIONS AND DATA REDUCTION

We have analyzed ALMA Band 6 archival data toward two YSOs in the Ophiuchus region taken as part of a Cycle 4 project<sup>1</sup>. Table 1 summarizes the coordinates and properties of our two target YSOs. Based on the infrared spectral indices, Oph-emb5 and Oph-emb9 are classified as Flat SED<sup>2</sup> and Class I, respectively.

Figure 1 shows the Wide-field Infrared Survey Explorer (WISE; Wright et al. 2010) images toward the two target YSOs. Oph-emb9 is irradiated by a luminous Herbig Be star S1 (also known as GSS35), located 2' ( $\sim 16800$  au) east of the  $\rho$  Oph A cloud (Lindberg

<sup>1</sup> project ID; 2016.1.00319.S, PI: Johan Lindberg

<sup>2</sup> A definition and characteristics are summarized in Evans et al. (2009).



**Table 1.** Summary of Target YSOs

Source	R.A. (J2000) <sup>a</sup>	Decl. (J2000) <sup>a</sup>	$L_{\text{bol}}$ ( $L_{\odot}$ ) <sup>b</sup>	$T_{\text{bol}}$ (K) <sup>c</sup>	$M_{\text{env}}$ ( $M_{\odot}$ ) <sup>d</sup>	$\alpha_{\text{IR}}$ <sup>e</sup>	Class <sup>f</sup>
Oph-emb5	16 <sup>h</sup> 27 <sup>m</sup> 21 <sup>s</sup> .96	-24°27′27″.7	0.1 (0.1)	87 (28)	0.15 (0.01)	-0.05 (0.05)	Flat
Oph-emb9	16 <sup>h</sup> 26 <sup>m</sup> 25 <sup>s</sup> .44	-24°23′01″.3	0.12 (0.37)	135 (49)	0.65 (0.05)	0.87 (0.05)	I

NOTE—Numbers in parentheses indicate uncertainties corrected by the distances.

<sup>a</sup>Coordinates of infrared sources determined by the Spitzer observations (Enoch et al. 2009).

<sup>b</sup>Bolometric luminosities at a distance of 125 pc taken from Enoch et al. (2009) and scaled to the newly measured distances (140.2 pc and 138.6 pc for Oph-emb5 and Oph-emb9, respectively; Ortiz-León et al. 2018).

<sup>c</sup>Bolometric temperature taken from Enoch et al. (2009).

<sup>d</sup>Envelope masses at a distance of 125 pc taken from Enoch et al. (2009) and scaled to the newly measured distances (140.2 pc and 138.6 pc for Oph-emb5 and Oph-emb9, respectively; Ortiz-León et al. 2018).

<sup>e</sup>IR spectral indexes ( $\alpha_{\text{IR}}$ ) taken from Enoch et al. (2009).

<sup>f</sup>Classification taken from White et al. (2015).

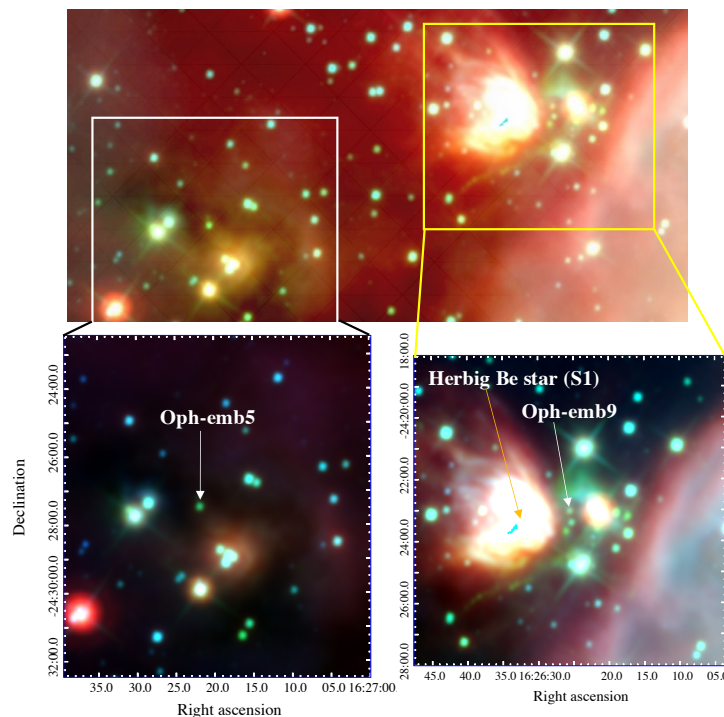


**Figure 1.** Wide-field Infrared Survey Explorer (WISE) images toward the two target YSOs; blue; W1 ( $3.4 \mu\text{m}$ ), green; W2 ( $4.6 \mu\text{m}$ ), red; W4 ( $22 \mu\text{m}$ ), respectively. The color scales are different and have been adjusted for each panel.

et al. 2017). This Herbig Be star has spectral class of B4 (Bouvier & Appenzeller 1992) and luminosity of  $\sim 1000 - 1600 L_{\odot}$  (Bontemps et al. 2001; Wilking et al. 2005). On the other hand, Oph-emb5 is located in a relatively isolated region and is not affected by any other sources.

The data sets contain the 12-m array, 7-m array, and Total Power (TP) data. The 12-m array and 7-m array data were obtained in 2017 March. The TP observations were carried out in 2016 October toward Oph-

emb9, and 2016 November and December, 2017 March and April toward Oph-emb5. Coordinates of the phase reference centers are  $(\alpha_{J2000}, \delta_{J2000}) = (16^{\text{h}}27^{\text{m}}21^{\text{s}}.83, -24^{\circ}27'27''.6)$  and  $(16^{\text{h}}26^{\text{m}}25^{\text{s}}.49, -24^{\circ}23'01''.6)$  toward Oph-emb5 and Oph-emb9, respectively.

Table 2 summarizes the details of each spectral window. The correlator setup with a frequency resolution of 61 kHz was used for molecular line observations. This frequency resolution corresponds to a velocity resolution of  $\sim 0.084 \text{ km s}^{-1}$ . The velocity resolutions for each re-

**Table 2.** Summary of spectral windows covered by the correlator setup

Frequency Range (GHz)	Molecule	Transition	$\Delta v^a$ ( $\text{km s}^{-1}$ )
217.92–217.96	<i>c</i> -C <sub>3</sub> H <sub>2</sub>	5 <sub>1,4</sub> – 4 <sub>2,3</sub>	0.084
217.80–217.84	<i>c</i> -C <sub>3</sub> H <sub>2</sub>	6 <sub>0,6</sub> – 5 <sub>1,5</sub>	0.084
218.20–218.24	H <sub>2</sub> CO	3 <sub>0,3</sub> – 2 <sub>0,2</sub>	0.2
218.45–218.49	H <sub>2</sub> CO	3 <sub>2,2</sub> – 2 <sub>2,1</sub>	0.084/0.2 <sup>b</sup>
218.74–218.78	H <sub>2</sub> CO	3 <sub>2,1</sub> – 2 <sub>2,0</sub>	0.084/0.2 <sup>b</sup>
218.42–218.46	CH <sub>3</sub> OH	4 <sub>-2,3</sub> – 3 <sub>-1,2</sub> <i>E</i>	0.084/0.2 <sup>b</sup>
219.54–219.58	C <sup>18</sup> O	2 – 1	0.2
220.38–220.41	<sup>13</sup> CO	2 – 1	0.2
216.09–216.13	DCO <sup>+</sup>	3 – 2	0.084
217.22–217.26	DCN	3 – 2	0.084
216.0–218.0	Continuum		...

<sup>a</sup>Velocity resolution of the resultant cubes.

<sup>b</sup>The velocity resolution of 0.084  $\text{km s}^{-1}$  and 0.2  $\text{km s}^{-1}$  were applied for Oph-emb5 and Oph-emb9 data, respectively.

sultant cube are also summarized in Table 2. We employed a velocity resolution of 0.2  $\text{km s}^{-1}$ , when lines can be resolved sufficiently by this velocity resolution. The fields of views (FoV) of the 12-m array and 7-m array are  $\sim 27''$  and  $\sim 46''$ , respectively.

We carried out data reduction and imaging using the Common Astronomy Software Application (CASA [McMullin et al. 2007](#)) on the pipeline-calibrated visibilities. We ran the calibration scripts using CASA version 4.7.0 for all of the data except for the TP data toward Oph-emb5, which was run with version 4.7.2.

The interferometric data cubes were created using the CASA “tclean” task after concatenating, combining the 12-m array and 7-m array data by task “concat”. Briggs weighting with a robust parameter of 0.5 was applied. The TP images were made using the “sdimaging” task. We combined the interferometer data with the TP data by using the feather task in CASA. We applied an sdfactor of 1.2. We conducted the primary beam correction for the combined images. The resulting angular resolutions are approximately  $2''.2 \times 1''.5$  and  $1''.8 \times 1''.3$  in Oph-emb5 and Oph-emb9, respectively. These angular resolutions correspond to 308 au  $\times$  210 au in Oph-emb5 and 249 au  $\times$  180 au in Oph-emb9 at the source distances (140.2 pc and 138.6 pc for Oph-emb5 and Oph-emb9, respectively; [Ortiz-León et al. 2018](#)).

Continuum images ( $\lambda = 1.38$  mm) with the 12-m array data were made by tclean task with the specmode of “mfs” in CASA. The center frequency and band width for these continuum data are 217.0 GHz and 2 GHz, respectively. The resulting angular resolutions are  $2''.2 \times 1''.5$  and  $1''.8 \times 1''.3$  for Oph-emb5 and Oph-emb9, respectively. The noise levels of the continuum images are  $6.0 \times 10^{-2}$  mJy beam<sup>-1</sup> and 1.0 mJy beam<sup>-1</sup> for Oph-emb5 and Oph-emb9, respectively.

### 3. RESULTS AND ANALYSES

#### 3.1. Continuum images

The continuum images toward the two YSOs are shown in Figure 2. The yellow crosses indicate the positions of infrared (IR) sources identified by the Spitzer Core to Disk (c2d) Legacy program ([Enoch et al. 2009](#)). Continuum emission is detected toward the YSO Oph-emb9. On the other hand, no continuum emission was detected toward the YSO Oph-emb5. [Kamazaki et al. \(2019\)](#) also did not detect the continuum emission toward this source (J162721 in their paper) at the 1.3 mm wavelength using ALMA. The non-detection of dust continuum emission has also been reported toward other Class I YSOs (e.g., [Taniguchi et al. 2021b](#)).

#### 3.2. Moment 0 maps of the observed molecular lines

Figures 3 and 4 show moment 0 maps of the observed molecular lines toward Oph-emb5 and Oph-emb9, respectively. Table 3 summarizes information on the noise levels for each panel.

Around Oph-emb5, there are differences in spatial distributions between carbon-chain species (*c*-C<sub>3</sub>H<sub>2</sub>) and COMs (H<sub>2</sub>CO and CH<sub>3</sub>OH). The hydrocarbon *c*-C<sub>3</sub>H<sub>2</sub> is enhanced in the region west of the IR source (shown in panels (a) and (b) in Figure 3). On the other hand, H<sub>2</sub>CO and CH<sub>3</sub>OH tend to be enhanced to the east of the IR source. The H<sub>2</sub>CO (3<sub>0,3</sub> – 2<sub>0,2</sub>) line (panel (c)) is more extended than its other lines (panels (d) and (e)). This seems to be caused by the different upper-state energies (Table 3). The peaks of CH<sub>3</sub>OH are consistent with those of H<sub>2</sub>CO. Peaks of C<sup>18</sup>O and <sup>13</sup>CO (panels (g) and (h)) are located at the north-east edge and their spatial distributions resemble that of H<sub>2</sub>CO (3<sub>0,3</sub> – 2<sub>0,2</sub>) line. The DCO<sup>+</sup> moment 0 map shows an extended structure (panel (i)). We did not detect the DCN line toward Oph-emb5 (panel (j)).

In Oph-emb9, the observed molecular emission for all detected lines is enhanced in the eastern part of the FoV. This side is irradiated by the nearby Herbig Be star (Figure 1). More details are discussed in Section 3.2.1.

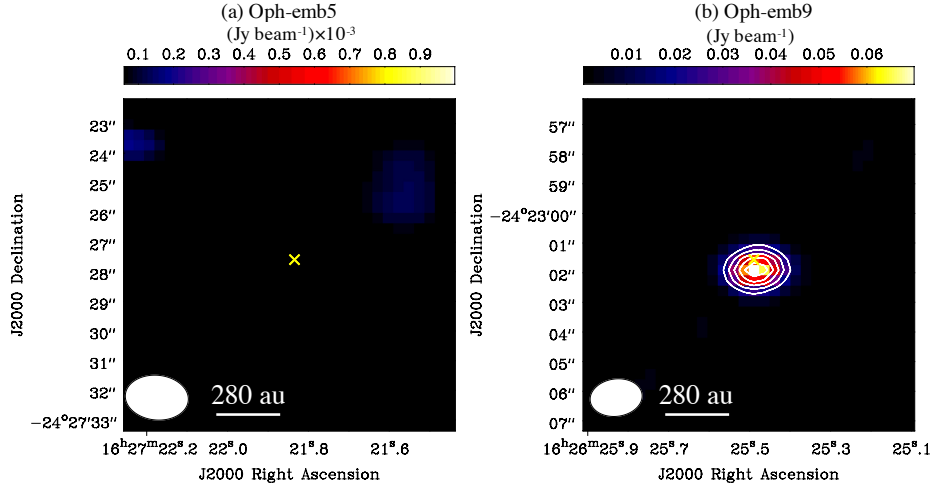


**Figure 2.** Continuum images ( $\lambda = 1.38$  mm) toward (a) Oph-emb5 and (b) Oph-emb9, respectively. The contour levels are 20, 40, 50, 60 times of the rms noise level, which are  $6.0 \times 10^{-2}$  mJy beam $^{-1}$  and  $1.0$  mJy beam $^{-1}$  for panels (a) and (b), respectively. The yellow crosses indicate positions of the infrared sources (Enoch et al. 2009). The filled white ellipses indicate the beam sizes of  $2''.2 \times 1''.5$  and  $1''.8 \times 1''.3$  for panels (a) and (b), respectively.

**Table 3.** Summary of the moment 0 maps

Panel	Species	Transition	Rest Frequency (GHz)	$E_{\text{up}}/k$ (K)	rms <sup>a</sup>	
					Oph-emb5	Oph-emb9
(a)	<i>c</i> -C <sub>3</sub> H <sub>2</sub>	5 <sub>1,4</sub> – 4 <sub>2,3</sub>	217.940046	35.4	1.3	2.5
(b)	<i>c</i> -C <sub>3</sub> H <sub>2</sub>	6 <sub>0,6</sub> – 5 <sub>1,5</sub>	217.822148	38.6	1.0	3.2
(c)	H <sub>2</sub> CO	3 <sub>0,3</sub> – 2 <sub>0,2</sub>	218.222192	21.0	2.4	6.9
(d)	H <sub>2</sub> CO	3 <sub>2,2</sub> – 2 <sub>2,1</sub>	218.475632	68.1	1.8	6.1
(e)	H <sub>2</sub> CO	3 <sub>2,1</sub> – 2 <sub>2,0</sub>	218.760066	68.1	1.3	5.5
(f)	CH <sub>3</sub> OH	4 <sub>-2,3</sub> – 3 <sub>-1,2</sub> <i>E</i>	218.440063	45.5	1.5	5.1
(g)	C <sup>18</sup> O	2 – 1	219.5603541	15.8	3.5	6.4
(h)	<sup>13</sup> CO	2 – 1	220.3986842	15.9	5.6	10.9
(i)	DCO <sup>+</sup>	3 – 2	216.1125822	20.7	1.5	3.4
(j)	DCN	3 – 2	217.2385378	20.9	3.1	3.8

<sup>a</sup>Unit is mJy beam $^{-1}$  km s $^{-1}$ .

NOTE—Transition, rest frequency, and upper-state energy are taken from the Cologne Database for Molecular Spectroscopy (CDMS; Müller et al. 2005).

H<sub>2</sub>CO shows an elongated feature from the northeast to the southwest. The CH<sub>3</sub>OH emission shows a similar tendency as H<sub>2</sub>CO, and their peaks are consistent with each other. In addition, a weak CH<sub>3</sub>OH peak is associated with the IR source. The emission from C<sup>18</sup>O and <sup>13</sup>CO is generally strong in the eastern edge of the FoV, and <sup>13</sup>CO shows an additional, less strong and more concentrated, emission peak to the west. The orientation of the <sup>13</sup>CO emission peaks is consistent with the molecular outflow (Artur de la Villarmois et al. 2019). We have detected the DCN line toward Oph-emb9. Its

spatial distribution is the most compact and is different from the other deuterated species, DCO<sup>+</sup>. The upper state energy of the observed DCN line ( $E_{\text{up}}/k = 20.9$  K) is similar to that of DCO<sup>+</sup> (20.7 K), and it follows that the different spatial distributions are not caused by different excitation conditions. The details are discussed in Section 3.2.2.

### 3.2.1. Comparison of spatial distributions of *c*-C<sub>3</sub>H<sub>2</sub> with H<sub>2</sub>CO and CH<sub>3</sub>OH

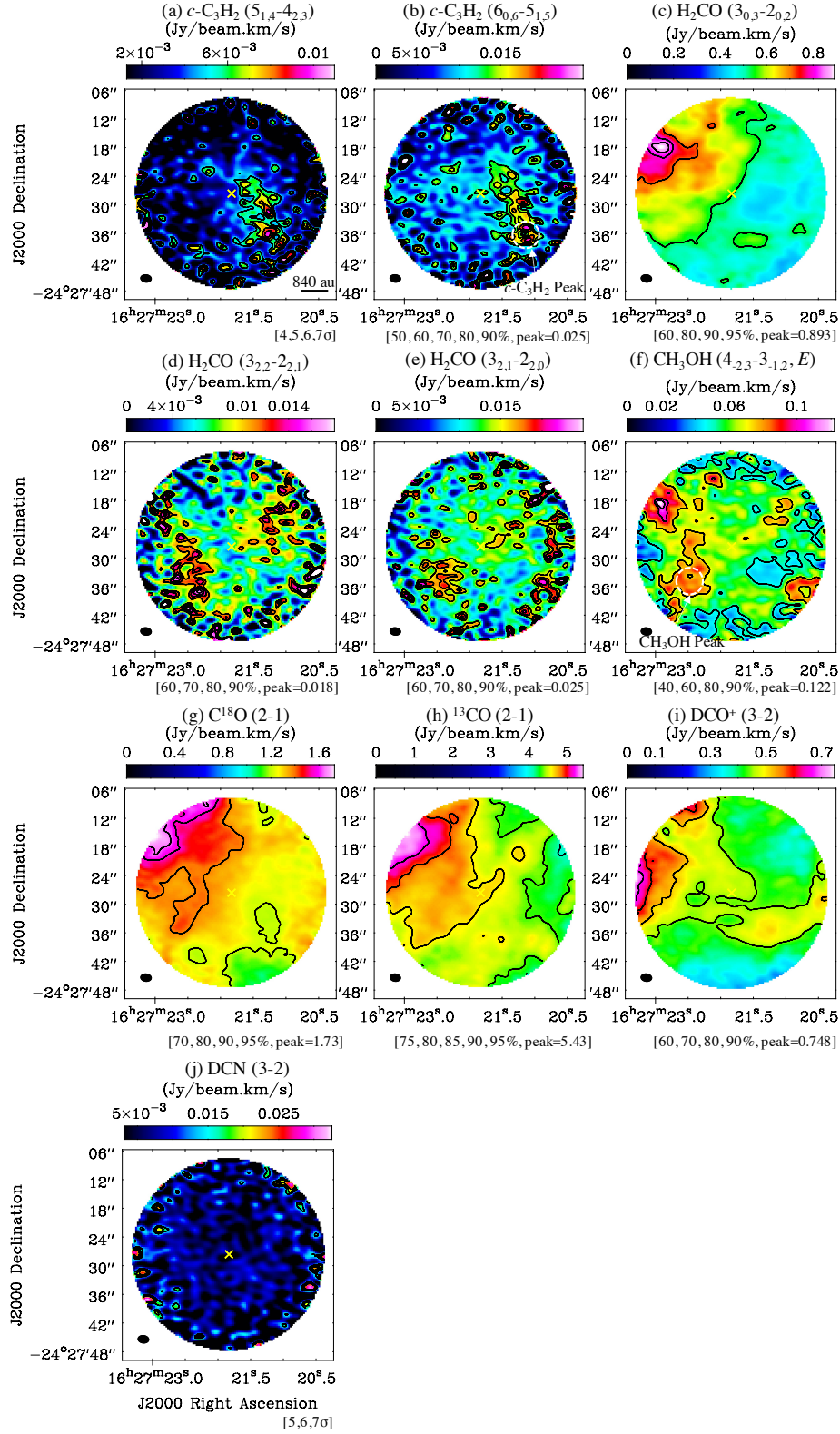


**Figure 3.** Moment 0 maps (combination of 12-m array, 7-m array, and TP) of  $c\text{-C}_3\text{H}_2$  in panels (a) and (b),  $\text{H}_2\text{CO}$  in panels (c)–(e),  $\text{CH}_3\text{OH}$  in panel (f),  $\text{C}^{18}\text{O}$  in panel (g),  $^{13}\text{CO}$  in panel (h),  $\text{DCO}^+$  in panel (i), and  $\text{DCN}$  in panel (j) toward Oph-emb5. The yellow crosses indicate positions of the infrared sources (Enoch et al. 2009). The contour levels are indicated in each panel at the bottom. The use of “ $\sigma$ ” means that contours are based on the rms noise level, and using “%” means contours relative to the peak intensity. The rms noise levels for each panel are summarized in Table 3. The filled black ellipses indicate the beam sizes of  $2''.2 \times 1''.5$ . In panels (b) and (f),  $c\text{-C}_3\text{H}_2$  Peak and  $\text{CH}_3\text{OH}$  Peak are indicated as white dashed circles (see Section 3.3).

In this subsection, we investigate effects of the UV radiation from the Herbig Be star on the chemistry around the observed YSOs by comparing the spatial distributions of  $c\text{-C}_3\text{H}_2$  with  $\text{H}_2\text{CO}$  and  $\text{CH}_3\text{OH}$ . In astrochemical models,  $c\text{-C}_3\text{H}_2$  can be formed by the destruction of large hydrocarbons through UV irradiation (top-down chemistry) or through the accumulation of C and H atoms to form small hydrocarbons (bottom-up chemistry) (Murillo et al. 2018). Large hydrocarbons could also be formed by destruction of dust grains (e.g., Zhen et al. 2014). In a more specific bottom-up chemistry, small hydrocarbons can be efficiently formed in the gas phase via ion-molecule reactions including  $\text{C}^+$  (e.g., Maluendes et al. 1993; Le Gal et al. 2017).

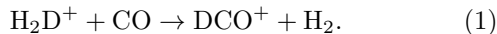
In the case of Oph-emb5,  $c\text{-C}_3\text{H}_2$  is enhanced at the west side, whereas  $\text{H}_2\text{CO}$  and  $\text{CH}_3\text{OH}$  are enhanced at the eastern parts relative to the YSO. Since Oph-emb5 is unlikely affected by any sources (Lindberg et al. 2017), these features are not induced by the UV radiation, but may indicate effects of stellar feedback, such as the molecular outflows. We discuss this point further in Section 3.4.1.

In Oph-emb9, the spatial distributions of  $c\text{-C}_3\text{H}_2$  show peaks at the eastern edge of the field, which is irradiated by the Herbig Be star. On the other hand, the spatial distributions of  $\text{H}_2\text{CO}$  and  $\text{CH}_3\text{OH}$  show maxima that are located farther from the Herbig Be star, and closer to the center of the field. The differences of the spatial distributions between small hydrocarbons and COMs in Oph-emb9 imply that top-down chemistry may efficiently contribute to the  $c\text{-C}_3\text{H}_2$  formation under conditions of UV irradiation.

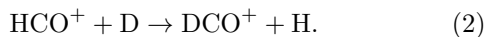
### 3.2.2. Comparison of spatial distributions of $\text{DCO}^+$ and $\text{DCN}$

In this subsection, we discuss the higher  $\text{DCO}^+$  column density in Oph-emb9 compared with Oph-emb5 and the sole  $\text{DCN}$  detection in Oph-emb9 as seen in their moment 0 maps.

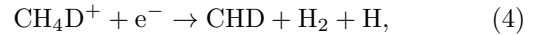
The  $\text{DCO}^+$  ion is considered to be formed in the gas phase mainly by the following reaction in cold environments ( $< 30$  K; Ceccarelli et al. 2014):



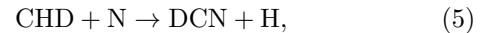
Another reaction that could produce  $\text{DCO}^+$  in warm regions ( $> 30$  K; Adams & Smith 1985) is:



In the case of  $\text{DCN}$ , the main formation pathways (Millar et al. 1989; Turner 2001) are:



followed by



or,



followed by Reaction (5). Hence,  $\text{DCN}$  is mainly formed by  $\text{CH}_2\text{D}^+$ . The  $\text{CH}_2\text{D}^+$  ion is formed by reaction between  $\text{CH}_3^+$  and  $\text{HD}$ , and the endothermicity of the back reaction is 654 K, which is higher than the reaction between  $\text{H}_3^+$  and  $\text{HD}$  (232 K) which forms  $\text{H}_2\text{D}^+$  (Öberg & Bergin 2021). As a result,  $\text{CH}_2\text{D}^+$  survives more easily in warmer gas ( $30 < T < 100$  K) compared to  $\text{H}_2\text{D}^+$  ( $< 30$  K; Ceccarelli et al. 2014). This means that  $\text{DCN}$  can efficiently form in warmer regions, whereas  $\text{DCO}^+$  can exist both in cold and warm regions due to Reactions (1) and (2).

In Oph-emb9, the UV radiation from the Herbig Be star can heat the gas and produce both the precursor ions  $\text{HCO}^+$  and  $\text{CH}_2\text{D}^+$  (Lindberg et al. 2017), leading to  $\text{DCO}^+$  (via Reaction (2),  $> 30$  K) and  $\text{DCN}$  (via Reactions (3) to (6),  $> 30$  K). In fact, the  $\text{DCN}$  spatial distribution follows that of the irradiated material, where the gas temperature is expected to be higher (Figure 4). On the other hand, in the case of Oph-emb5, the non-detection of  $\text{DCN}$  results from lower-temperature conditions, which implies formation of  $\text{DCO}^+$  via Reaction (1) ( $< 30$  K). The lower column density of  $\text{DCO}^+$  in Oph-emb5 compared to Oph-emb9 corresponds to lower  $\text{H}_2\text{D}^+$  abundance due to weaker UV irradiation.

### 3.3. Spectral analysis

The spectral analysis of the detected lines of  $\text{H}_2\text{CO}$ ,  $\text{CH}_3\text{OH}$ ,  $c\text{-C}_3\text{H}_2$ ,  $\text{DCO}^+$ , and  $\text{DCN}$  was carried out using the CASSIS software (Vastel et al. 2015) together with the CDMS<sup>3</sup> and JPL<sup>4</sup> spectroscopic databases. For the spectral analysis, we constructed  $6''$  (840 au) beam average spectra to balance the angular resolution and sensitivity. We pick two positions around each YSO, which are the strong  $c\text{-C}_3\text{H}_2$  emission positions, and the strong  $\text{CH}_3\text{OH}$  emission positions. They are chosen because each position seems to represent different chemical features. We indicate these locations as “ $c\text{-C}_3\text{H}_2$  Peak” and “ $\text{CH}_3\text{OH}$  Peak”, respectively. Panels (b) and (f) in Figures 3 and 4 indicate the positions and the beam ( $6''$ ) used for spectral analysis.

We applied the Markov chain Monte Carlo (MCMC) method assuming the local thermodynamic equilibrium

<sup>3</sup> <https://cdms.astro.uni-koeln.de>

<sup>4</sup> <https://spec.jpl.nasa.gov>



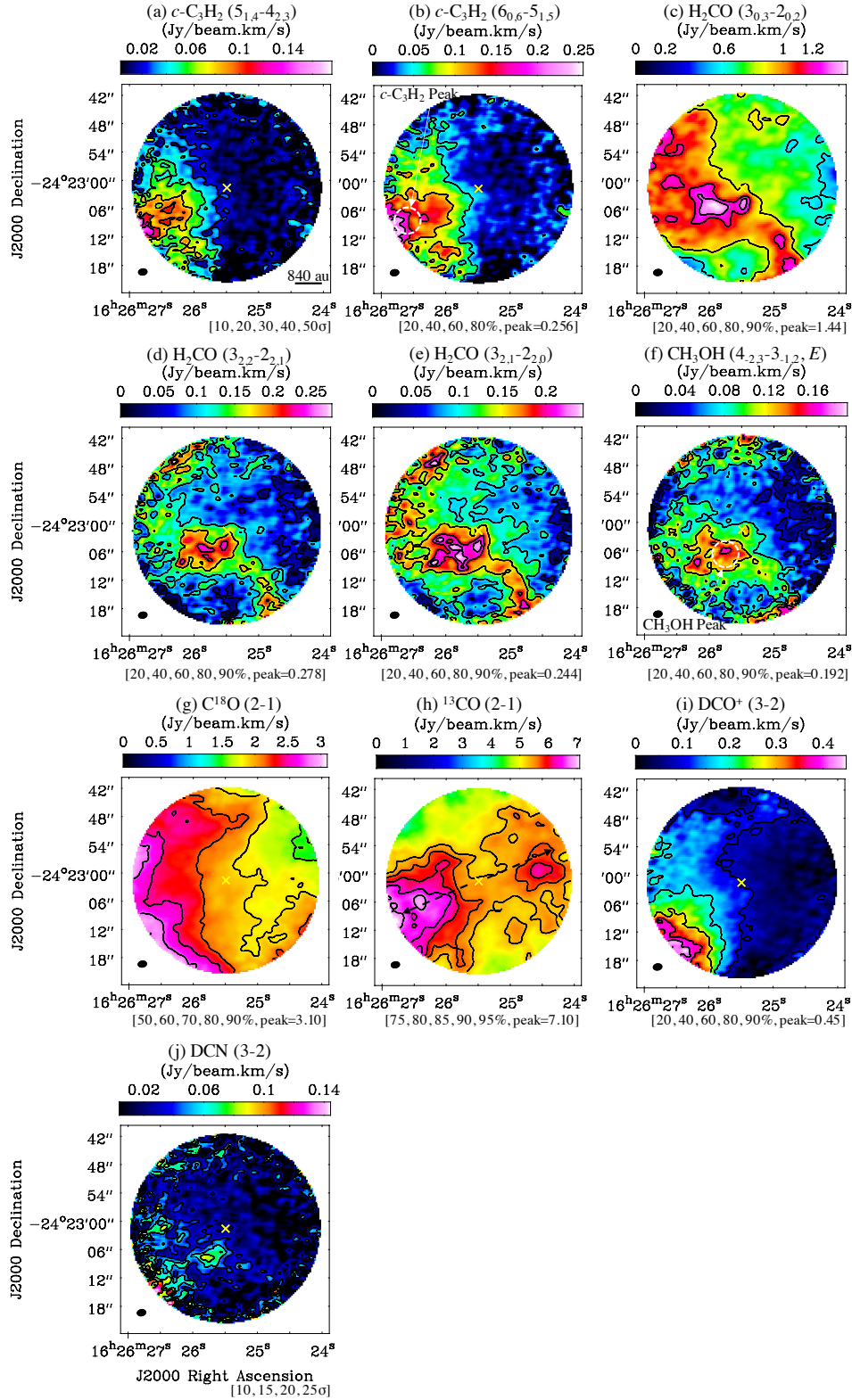


**Figure 4.** Moment 0 maps (combination of 12-m array, 7-m array, and TP) of  $c\text{-C}_3\text{H}_2$  in panels (a) and (b),  $\text{H}_2\text{CO}$  in panels (c)–(e),  $\text{CH}_3\text{OH}$  in panel (f),  $\text{C}^{18}\text{O}$  in panel (g),  $^{13}\text{CO}$  in panel (h),  $\text{DCO}^+$  in panel (i), and  $\text{DCN}$  in panel (j) toward Oph-emb9. The yellow crosses indicate positions of the infrared sources (Enoch et al. 2009). The contour levels are indicated in each panel at the bottom. The use of “ $\sigma$ ” means that contours are based on the rms noise level, and using “%” means contours relative to the peak intensity. The rms noise levels for each panel are summarized in Table 3. The filled black ellipses indicate the beam sizes of  $1''.8 \times 1''.3$ . In panels (b) and (f),  $c\text{-C}_3\text{H}_2$  Peak and  $\text{CH}_3\text{OH}$  Peak are indicated as white dashed circles (see Section 3.3). The black dashed arrows in panel (h) indicate the direction of the molecular outflow (Artur de la Villarmois et al. 2019).

(LTE) model in CASSIS. In this method, the column density ( $N$ ), excitation temperature ( $T_{\text{ex}}$ ), line width (FWHM), and radial velocity ( $V_{\text{LSR}}$ ) were treated as semi-free parameters within certain ranges, and solutions were obtained by a  $\chi^2$  minimization. The excitation temperatures of  $c\text{-C}_3\text{H}_2$  and  $\text{H}_2\text{CO}$  were derived to be  $8.7 \pm 1.0$  K and  $15.5 \pm 0.7$  K in Oph-emb5,  $9.9 \pm 0.3$  K and  $36.2 \pm 0.4$  K in Oph-emb9, respectively, based on APEX observations (Lindberg et al. 2017). We then set the excitation temperature range from 10 K to 40 K.

Table 4 summarizes fitting results. Since the  $\text{H}_2\text{CO}$  ( $3_{0,3} - 2_{0,2}$ ) line has different spatial distributions (Figures 3 and 4) and different upper state energies (Table 3) from the other two lines, these lines probably do not trace the same regions. We then derived parameters for  $\text{H}_2\text{CO}$  with the following two cases; (a) using the  $3_{0,3} - 2_{0,2}$  line, and (b) using the  $3_{2,2} - 2_{2,1}$  and  $3_{2,1} - 2_{2,0}$  lines.

Figures 5 and 6 show spectra at the  $c\text{-C}_3\text{H}_2$  peak and  $\text{CH}_3\text{OH}$  peak in Oph-emb5, and Figures 7 and 8 show spectra at each position in Oph-emb9. Purple curves indicate the fitted results (Table 4). The second velocity components may have been detected in the  $\text{H}_2\text{CO}$  and  $\text{CH}_3\text{OH}$  spectra, especially at the  $c\text{-C}_3\text{H}_2$  peak of Oph-emb5. However, we cannot fit these second components well with the current velocity resolution, and we therefore did not consider the second velocity component in our analyses. The radial velocities are almost consistent with previous APEX observations (Lindberg et al. 2017).

### 3.3.1. Comparison of the $N(c\text{-C}_3\text{H}_2)/N(\text{CH}_3\text{OH})$ ratio derived from CASSIS

UV radiation, if sufficiently intense, produces photon-dominated regions (PDRs). In PDR chemistry, small hydrocarbons such as  $c\text{-C}_3\text{H}_2$  can be abundant in less shielded regions (e.g.,  $A_v \sim 1.43$  mag; Tiwari et al. 2019), while  $\text{CH}_3\text{OH}$  formation is efficient in more shielded regions ( $A_v > 2$  mag; Esplugues et al. 2019). In order to investigate the effects of UV irradiation from the nearby Herbig Be star on Oph-emb9, we derive the  $N(c\text{-C}_3\text{H}_2)/N(\text{CH}_3\text{OH})$  ratio at each position as summarized in Table 4. The ratios at the  $c\text{-C}_3\text{H}_2$  Peak and the  $\text{CH}_3\text{OH}$  Peak in Oph-emb5 are derived to be  $0.015 \pm 0.003$  ( $1\sigma$ ) and  $0.006 \pm 0.003$ , and those in Oph-emb9 are calculated as  $0.37 \pm 0.06$  and  $0.020 \pm 0.011$ , respectively.

As a general trend, the  $N(c\text{-C}_3\text{H}_2)/N(\text{CH}_3\text{OH})$  ratios around Oph-emb9 are higher than those around Oph-emb5. This means that  $c\text{-C}_3\text{H}_2$  is relatively more abundant compared to  $\text{CH}_3\text{OH}$  in Oph-emb9. Hence, this

region may be affected by the UV radiation from the Herbig Be star.

We compare these ratios at the  $c\text{-C}_3\text{H}_2$  Peak and the  $\text{CH}_3\text{OH}$  Peak around each YSO. In the case of Oph-emb5, the  $N(c\text{-C}_3\text{H}_2)/N(\text{CH}_3\text{OH})$  ratio at the  $c\text{-C}_3\text{H}_2$  Peak is higher than that at the  $\text{CH}_3\text{OH}$  Peak by a factor of  $\sim 2.6$ . In Oph-emb9, the difference between the  $c\text{-C}_3\text{H}_2$  Peak and the  $\text{CH}_3\text{OH}$  Peak is a factor of  $\sim 18.5$ . Hence,  $c\text{-C}_3\text{H}_2$  is significantly enhanced at the  $c\text{-C}_3\text{H}_2$  Peak in Oph-emb9 compared to Oph-emb5. All of these results also support the PDR chemistry around Oph-emb9, which is likely driven by the nearby Herbig Be star. The PDR chemistry in this source was also suggested by the layered structures of CO and its isotopologues (Yamagishi et al. 2019). Our conclusion that the chemistry in the field of view of Oph-emb9 is strongly affected by the Herbig Be star is consistent with their results.

### 3.4. Moment 2 Maps of the $^{13}\text{CO}$ and $\text{C}^{18}\text{O}$ lines

Figure 9 shows moment 2 maps (velocity dispersion maps) of the  $^{13}\text{CO}$  ( $J = 2 - 1$ ) and  $\text{C}^{18}\text{O}$  ( $J = 2 - 1$ ) lines toward Oph-emb5 and Oph-emb9, respectively. In Appendix A, channel maps of these lines are presented in Figures 11–14. Around Oph-emb5, there are two velocity dispersion peaks in the  $^{13}\text{CO}$  moment 2 maps. The moment 2 maps of  $^{13}\text{CO}$  and  $\text{C}^{18}\text{O}$  are similar to each other around Oph-emb9; two dispersion maxima are located at the eastern and western positions, respectively.

#### 3.4.1. Comparisons of molecular distributions and velocity dispersion

In this subsection, we investigate the relationship between the chemical differentiation and velocity dispersion, which is an indicator of gas turbulent motions. Figure 10 shows comparisons of the  $^{13}\text{CO}$  moment 2 map (color scales) and the spatial distributions of  $\text{H}_2\text{CO}$  and  $c\text{-C}_3\text{H}_2$  (black contours). The black contours in the upper and bottom panels indicate moment 0 maps of the  $\text{H}_2\text{CO}$  ( $3_{0,3} - 2_{0,2}$ ) line and the  $c\text{-C}_3\text{H}_2$  ( $6_{0,6} - 5_{1,5}$ ) line, respectively.

There is no spatial relationship between the  $^{13}\text{CO}$  moment 2 map and the  $\text{H}_2\text{CO}$  moment 0 map around Oph-emb5, while the  $c\text{-C}_3\text{H}_2$  moment 0 map peaks at the location of the largest velocity dispersion position. The  $\text{H}_2\text{CO}$  emission may be associated with another source, which is located out of the field of view of these observations. However, we cannot determine from the current data set.

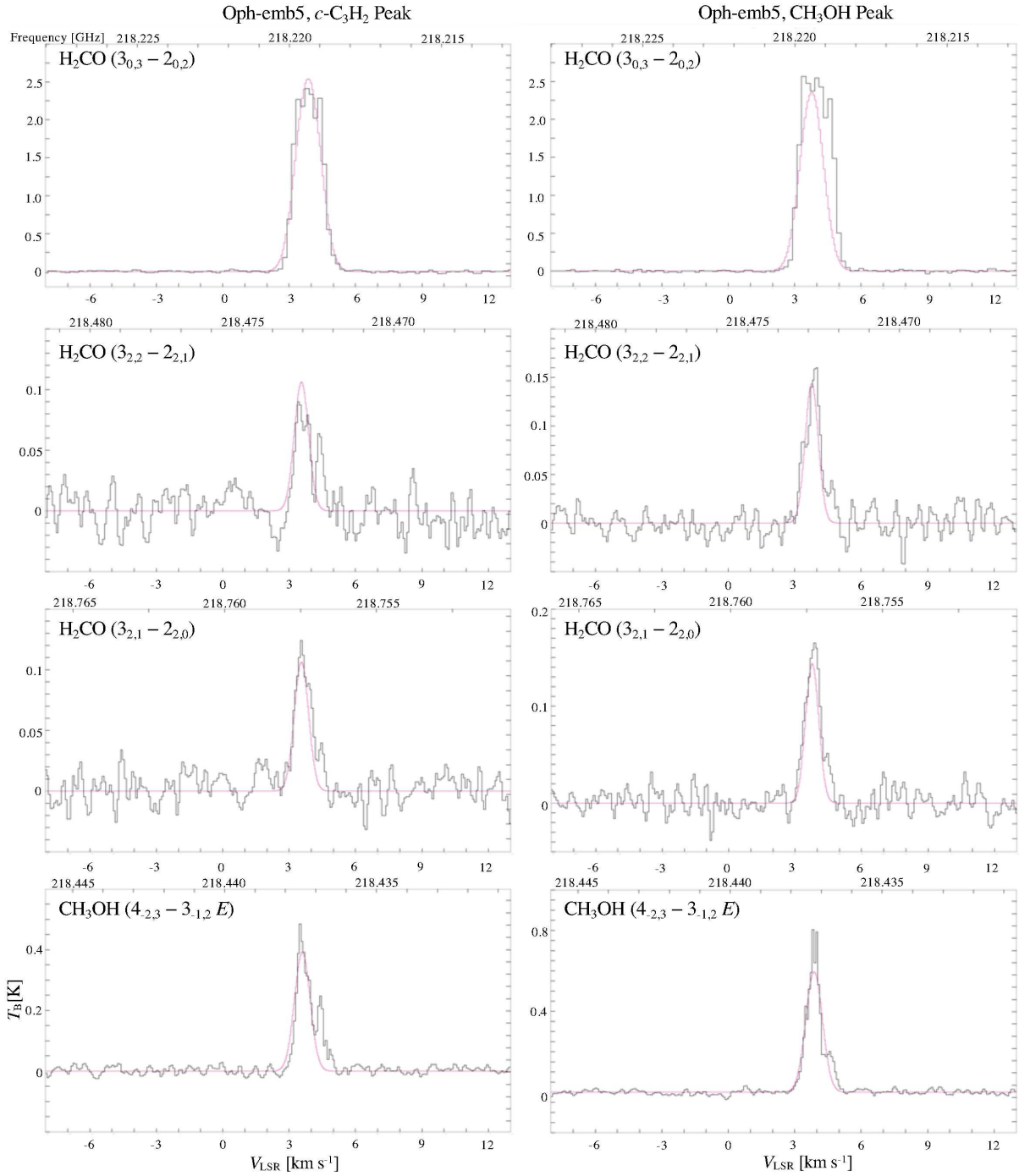
The peak of the  $\text{H}_2\text{CO}$  moment 0 map corresponds to the largest velocity dispersion position in the  $^{13}\text{CO}$  moment 2 map around Oph-emb9. These results may

Table 4. Summary of analytical results of spectra by CASSIS

Species	<i>c</i> -C <sub>3</sub> H <sub>2</sub> Peak				CH <sub>3</sub> OH Peak			
	<i>N</i> (cm <sup>-2</sup> )	<i>T</i> <sub>ex</sub> (K)	FWHM (km s <sup>-1</sup> )	<i>V</i> <sub>LSR</sub> (km s <sup>-1</sup> )	<i>N</i> (cm <sup>-2</sup> )	<i>T</i> <sub>ex</sub> (K)	FWHM (km s <sup>-1</sup> )	<i>V</i> <sub>LSR</sub> (km s <sup>-1</sup> )
<i>c</i> -C <sub>3</sub> H <sub>2</sub>	(7.7 ± 1.2) × 10 <sup>11</sup>	15.3 ± 2.2	0.57 ± 0.09	3.94 ± 0.04	(6.3 ± 1.0) × 10 <sup>11</sup>	12.0 ± 1.4	0.83 ± 0.11	3.93 ± 0.11
H <sub>2</sub> CO <sup>a</sup>	(2.9 ± 2.1) × 10 <sup>13</sup>	11.6 ± 0.9	1.36 ± 0.09	3.78 ± 0.09	(1.7 ± 0.5) × 10 <sup>13</sup>	16.7 ± 1.9	1.28 ± 0.07	3.763 ± 0.005
H <sub>2</sub> CO <sup>b</sup>	(5.6 ± 4.3) × 10 <sup>13</sup>	14.0 ± 3.6	0.78 ± 0.08	3.52 ± 0.08	(1.52 ± 0.08) × 10 <sup>13</sup>	17.8 ± 0.9	0.63 ± 0.07	3.765 ± 0.004
CH <sub>3</sub> OH	(5.3 ± 0.9) × 10 <sup>13</sup>	29.9 ± 4.7	0.84 ± 0.07	3.53 ± 0.08	(1.1 ± 0.5) × 10 <sup>14</sup>	21.0 ± 7.0	0.82 ± 0.07	3.87 ± 0.02
DCO <sup>+</sup>	(2.5 ± 0.2) × 10 <sup>12</sup>	11.7 ± 0.5	0.83 ± 0.02	3.98 ± 0.03	(4.4 ± 1.1) × 10 <sup>12</sup>	11.3 ± 0.6	0.73 ± 0.07	3.70 ± 0.18
<i>N</i> ( <i>c</i> -C <sub>3</sub> H <sub>2</sub> )/ <i>N</i> (CH <sub>3</sub> OH) <sup>c</sup>	0.015 ± 0.003				0.006 ± 0.003			
<b>Oph-emb5</b>								
<i>c</i> -C <sub>3</sub> H <sub>2</sub>	(6.7 ± 1.0) × 10 <sup>13</sup>	10.5 ± 0.3	0.59 ± 0.05	3.31 ± 0.10	(4.7 ± 2.5) × 10 <sup>12</sup>	12.3 ± 1.9	0.43 ± 0.04	3.30 ± 0.09
H <sub>2</sub> CO <sup>a</sup>	(1.24 ± 0.06) × 10 <sup>14</sup>	38.3 ± 0.7	1.31 ± 0.01	3.12 ± 0.05	(1.54 ± 0.06) × 10 <sup>14</sup>	33.7 ± 1.8	1.40 ± 0.04	3.28 ± 0.10
H <sub>2</sub> CO <sup>b</sup>	(8.1 ± 0.9) × 10 <sup>13</sup>	38.3 ± 1.2	1.36 ± 0.10	3.19 ± 0.12	(2.2 ± 0.5) × 10 <sup>14</sup>	26.2 ± 5.3	1.03 ± 0.09	3.39 ± 0.05
CH <sub>3</sub> OH	(1.8 ± 0.1) × 10 <sup>14</sup>	35.9 ± 2.6	0.97 ± 0.04	3.15 ± 0.03	(2.4 ± 0.2) × 10 <sup>14</sup>	34.4 ± 3.1	1.02 ± 0.05	3.28 ± 0.04
DCO <sup>+</sup>	(1.1 ± 0.8) × 10 <sup>13</sup>	11.2 ± 0.5	0.40 ± 0.08	3.26 ± 0.11	(9.3 ± 3.2) × 10 <sup>11</sup>	11.0 ± 0.5	0.56 ± 0.04	3.40 ± 0.06
DCN	(9.4 ± 1.7) × 10 <sup>11</sup>	10.5 ± 0.2	0.69 ± 0.03	3.23 ± 0.01	(7.3 ± 0.7) × 10 <sup>11</sup>	10.5 ± 0.2	0.85 ± 0.06	3.58 ± 0.03
<i>N</i> ( <i>c</i> -C <sub>3</sub> H <sub>2</sub> )/ <i>N</i> (CH <sub>3</sub> OH) <sup>c</sup>	0.37 ± 0.06				0.020 ± 0.011			

NOTE—The errors are the standard deviation.

<sup>a</sup>The values are derived from fitting of the 3<sub>0,3</sub> – 2<sub>0,2</sub> line.<sup>b</sup>The values are derived from fitting of the 3<sub>2,2</sub> – 2<sub>2,1</sub> and 3<sub>2,1</sub> – 2<sub>2,0</sub> lines.<sup>c</sup>The errors are calculated from the standard deviation of the column densities.



**Figure 5.** Spectra of  $\text{H}_2\text{CO}$  and  $\text{CH}_3\text{OH}$  toward Oph-emb5. Purple curves indicate the fitted results obtained using the CASSIS software.

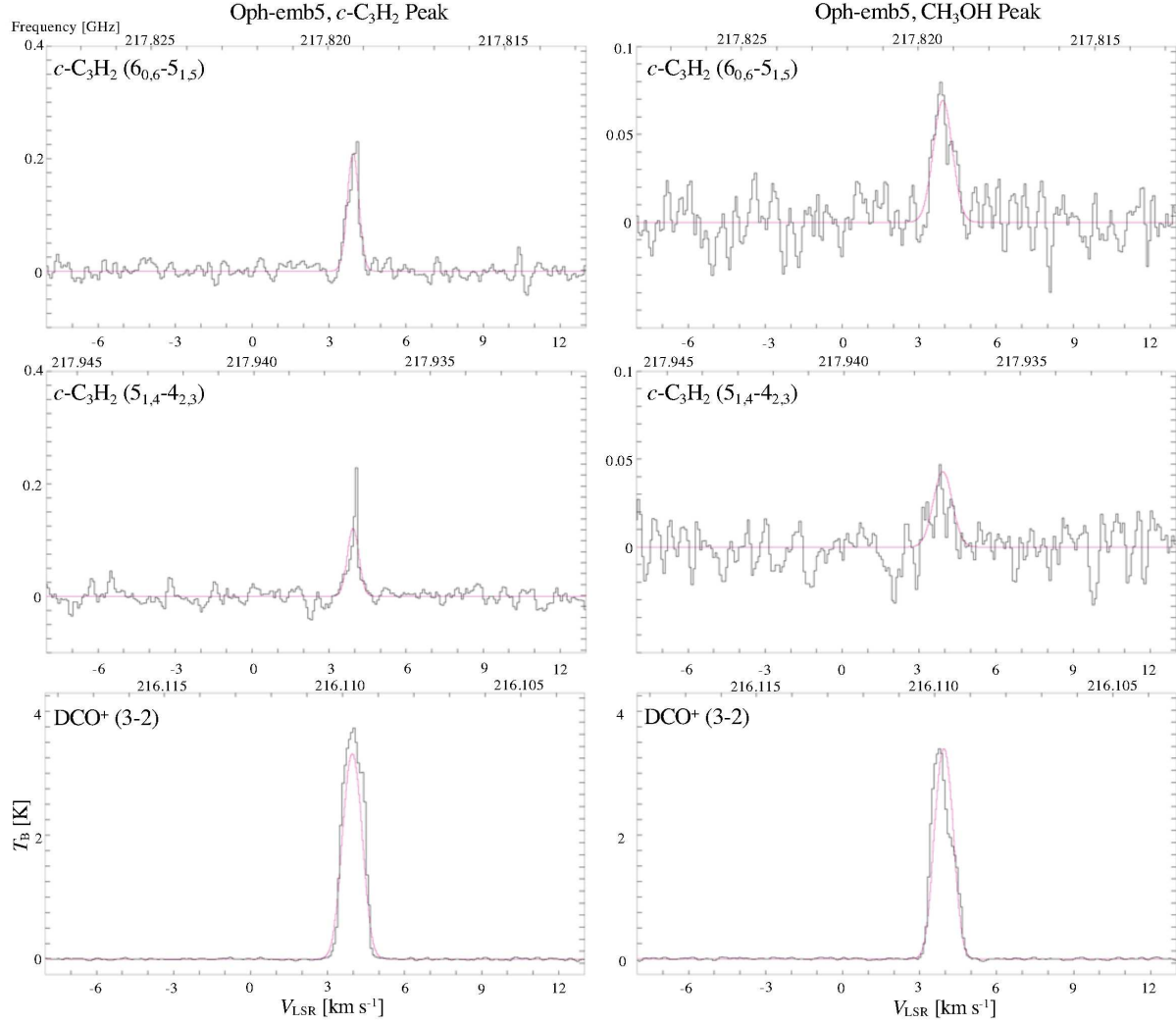


**Figure 6.** Spectra of  $c\text{-C}_3\text{H}_2$  and  $\text{DCO}^+$  toward Oph-emb5. Purple curves indicate the fitted results obtained using the CASSIS software.

suggest that COMs ( $\text{H}_2\text{CO}$  and  $\text{CH}_3\text{OH}$ ) are enhanced by the shock chemistry induced by the nearby Herbig Be star or the molecular outflow originated from the Oph-emb9 YSO (White et al. 2015). Large-scale enhancement of  $\text{CH}_3\text{OH}$  by shock has been reported in other cluster-forming regions (e.g., Taniguchi et al. 2020). The  $\text{H}_2\text{CO}$  emission is strongly enhanced in the eastern direction from the IR source, while the enhancement is not efficient on the opposite side. If the molecular outflow is the sole source of the enhancement of these COMs, this spatial difference cannot be explained. An alternative explanation is that a strong shock region at the eastern position is produced by a combination of the molecular outflow from Oph-emb9 and the effect of gas compression from the Herbig Be star.

The peak in the  $c\text{-C}_3\text{H}_2$  moment 0 map does not coincide with the peak in the  $^{13}\text{CO}$  moment 2 map. As

mentioned in Section 3.3.1, the PDR chemistry seems to enhance  $c\text{-C}_3\text{H}_2$  around Oph-emb9, and the shock chemistry is unlikely related to the formation of  $c\text{-C}_3\text{H}_2$ . In fact, the line widths of  $\text{H}_2\text{CO}$  and  $\text{CH}_3\text{OH}$  are larger than that of  $c\text{-C}_3\text{H}_2$  (see Table 4). In summary, the chemical processes around Oph-emb9 are strongly affected by the nearby Herbig Be star, the UV radiation and probably gas compression.

#### 4. CONCLUSIONS

We present Band 6 ALMA Cycle 4 archival data toward two YSOs in the Ophiuchus region. Oph-emb9 is irradiated by a nearby Herbig Be star, while Oph-emb5 is located in a relatively quiescent region. Using the data, we investigate effects from a nearby bright star on the chemistry around the target YSOs. The high angular resolution data with ALMA enable us to inves-



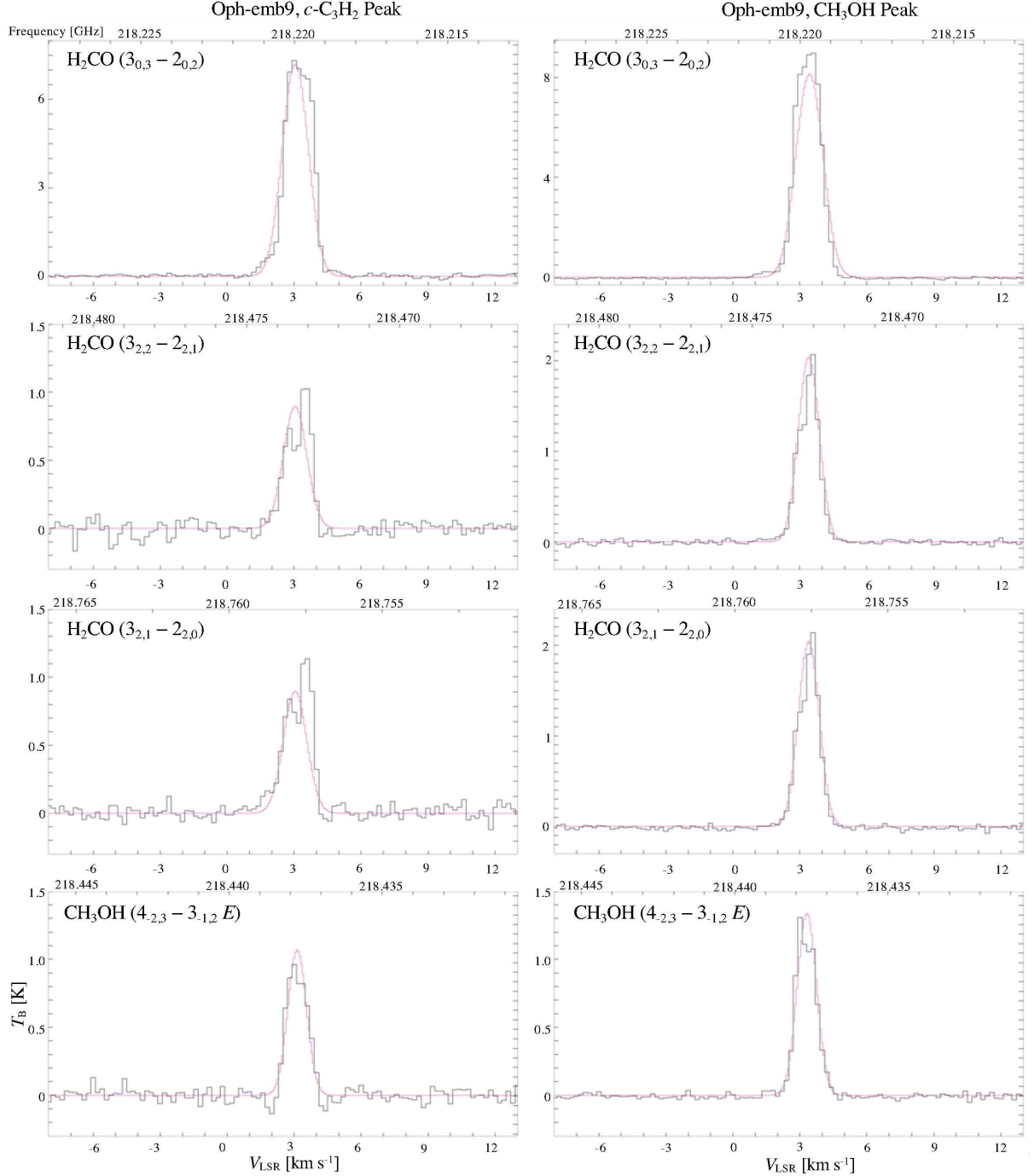


**Figure 7.** Spectra toward of  $\text{H}_2\text{CO}$  and  $\text{CH}_3\text{OH}$  Oph-emb9. Purple curves indicate the fitted results obtained using the CASSIS software.

tigate the chemical processes in more detail compared to previous single-dish data (Lindberg et al. 2017).

We have detected  $c\text{-C}_3\text{H}_2$ ,  $\text{H}_2\text{CO}$ ,  $\text{CH}_3\text{OH}$ ,  $^{13}\text{CO}$ ,  $\text{C}^{18}\text{O}$ ,  $\text{DCO}^+$ , and  $\text{DCN}$  in Oph-emb9, and all of them except for  $\text{DCN}$  in Oph-emb5. The small hydrocarbon  $c\text{-C}_3\text{H}_2$  and COMs ( $\text{H}_2\text{CO}$  and  $\text{CH}_3\text{OH}$ ) show different spatial distributions around both YSOs, which indicate the chemical differentiation.

The  $N(c\text{-C}_3\text{H}_2)/N(\text{CH}_3\text{OH})$  column density ratios around Oph-emb9 are higher than those around Oph-emb5. Furthermore,  $c\text{-C}_3\text{H}_2$  is greatly enhanced at its peak position, which is irradiated by the Herbig Be star. These results indicate the PDR chemistry around the Oph-emb9 YSO driven by the Herbig Be star.

We compare the moment 0 maps of  $c\text{-C}_3\text{H}_2$  and  $\text{H}_2\text{CO}$  with the  $^{13}\text{CO}$  moment 2 maps. In the case of Oph-

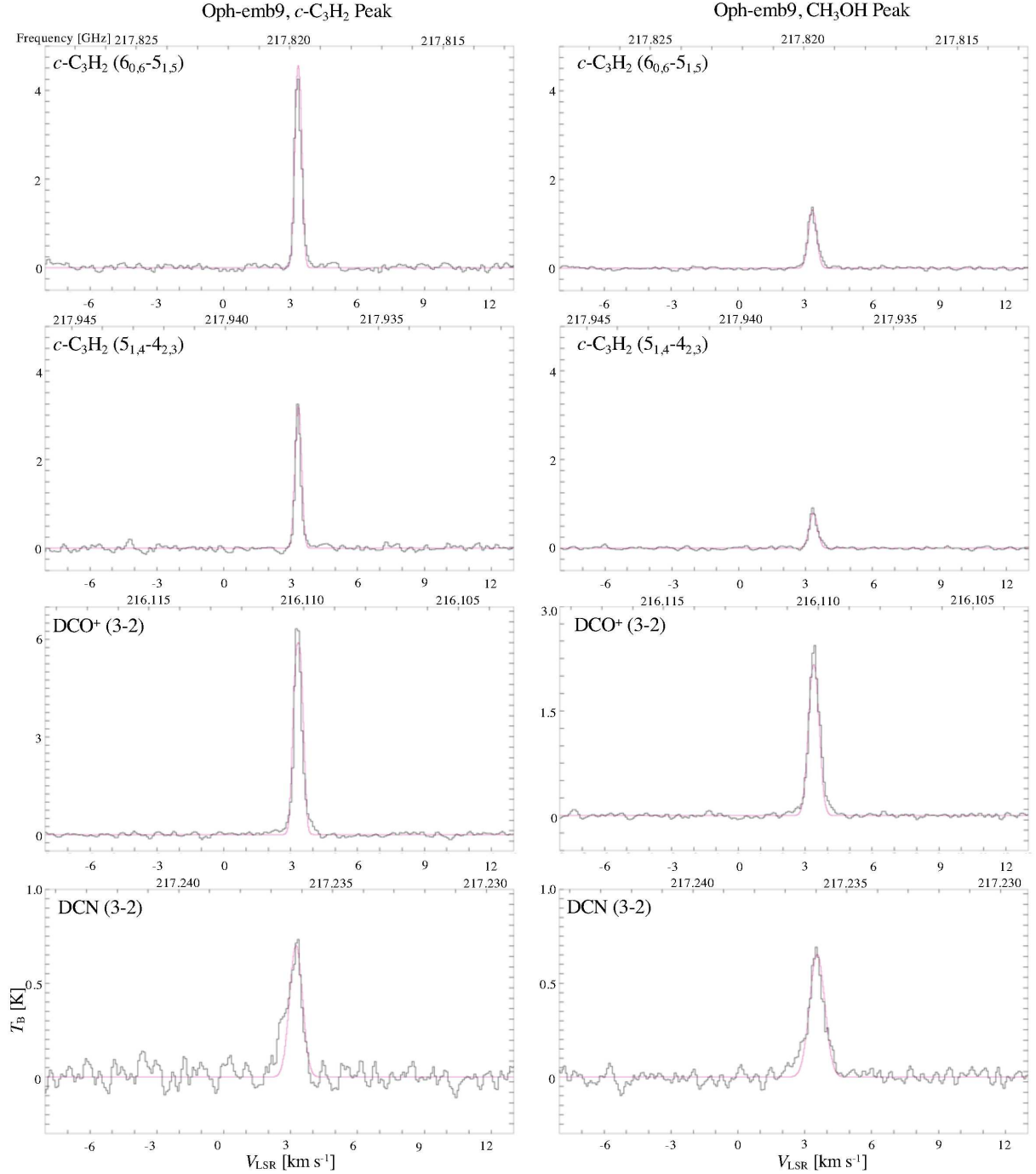


**Figure 8.** Spectra  $c\text{-C}_3\text{H}_2$ ,  $\text{DCO}^+$ , and  $\text{DCN}$  toward Oph-emb9. Purple curves indicate the fitted results obtained using the CASSIS software.

emb5, the peak position of the  $c\text{-C}_3\text{H}_2$  moment 0 map corresponds to the position with the largest velocity dispersion in the  $^{13}\text{CO}$  moment 2 map. Moreover, the peak of the  $\text{H}_2\text{CO}$  moment 0 map is consistent with the position with the largest velocity dispersion in Oph-emb9. Such results imply that shock chemistry enhances the gas-phase COMs around Oph-emb9. The strong shock

seems to be induced by a combination of the nearby Herbig Be star and the molecular outflow from Oph-emb9 itself.

We have investigated the higher  $\text{DCO}^+$  column density and the detection of  $\text{DCN}$  in Oph-emb9. The main formation pathway of  $\text{DCO}^+$  around Oph-emb9 seems to be the reaction  $\text{HCO}^+ + \text{D} \rightarrow \text{DCO}^+ + \text{H}$  in rela-

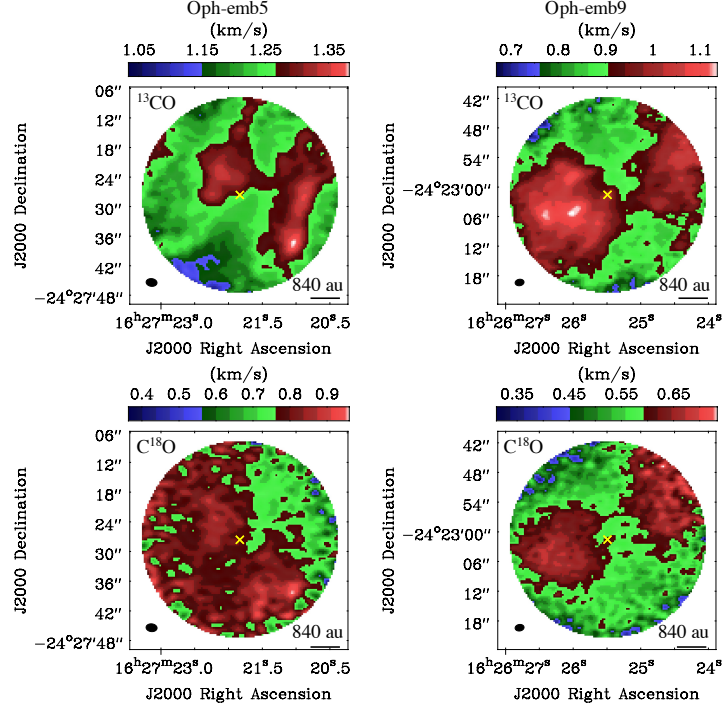


**Figure 9.** Moment 2 maps of the  $^{13}\text{CO}$  ( $J = 2 - 1$ ) and  $\text{C}^{18}\text{O}$  ( $J = 2 - 1$ ) lines in upper panels and bottom panels, respectively. Left and right panels show results for Oph-emb5 and Oph-emb9, respectively. The velocity ranges used in the  $^{13}\text{CO}$  and  $\text{C}^{18}\text{O}$  maps are  $-1.2 - +6 \text{ km s}^{-1}$  and  $-0.6 - +5.8 \text{ km s}^{-1}$  in Oph-emb5, and  $0 - +6.4 \text{ km s}^{-1}$  and  $+0.8 - +5.6 \text{ km s}^{-1}$  in Oph-emb9, respectively. The yellow crosses indicate positions of the infrared sources (Enoch et al. 2009). The filled black ellipses indicate the angular resolutions of  $2''.2 \times 1''.5$  and  $1''.8 \times 1''.3$  for Oph-emb5 and Oph-emb9, respectively.

tively warm region ( $30 < T < 100 \text{ K}$ ). This is supported by the detection of DCN, which is expected to be formed in warm regions. In addition, the UV radiation from the Herbig Be star can enhance the gas-phase  $\text{HCO}^+$  abundance with ion-molecule chemistry. On the other hand, the dominant formation pathway of  $\text{DCO}^+$  around Oph-emb5 is the reaction of  $\text{H}_2\text{D}^+ + \text{CO} \rightarrow \text{DCO}^+ + \text{H}_2$ , which can proceed only in cold regions ( $< 30 \text{ K}$ ).

This paper makes use of the following ALMA data: ADS/JAO.ALMA#2016.1.00319.S. ALMA is a partnership of ESO (representing its member states), NSF (USA) and NINS (Japan), together with NRC (Canada), MOST and ASIAA (Taiwan), and KASI (Republic of Korea), in cooperation with the Republic of Chile. The Joint ALMA Observatory is operated by ESO, AUI/NRAO and NAOJ. This work included analyses carried out with the CASSIS software and the CDMS and JPL spectroscopic databases. CASSIS has been developed by IRAP-UPS/CNRS (<http://cassis.irap.omp.eu>). This work was supported by JSPS KAKENHI grant No. JP20K14523. K.T. acknowledges support from Japan Foundation for Promotion of Astronomy. This research was carried out in part at the Jet Propulsion Laboratory, which is operated for NASA by the California Institute of Technology. E.H. thanks the National Science Foundation for support through grant AST-1906489. We thank the anonymous referee whose valuable comments helped improve the quality of the paper.

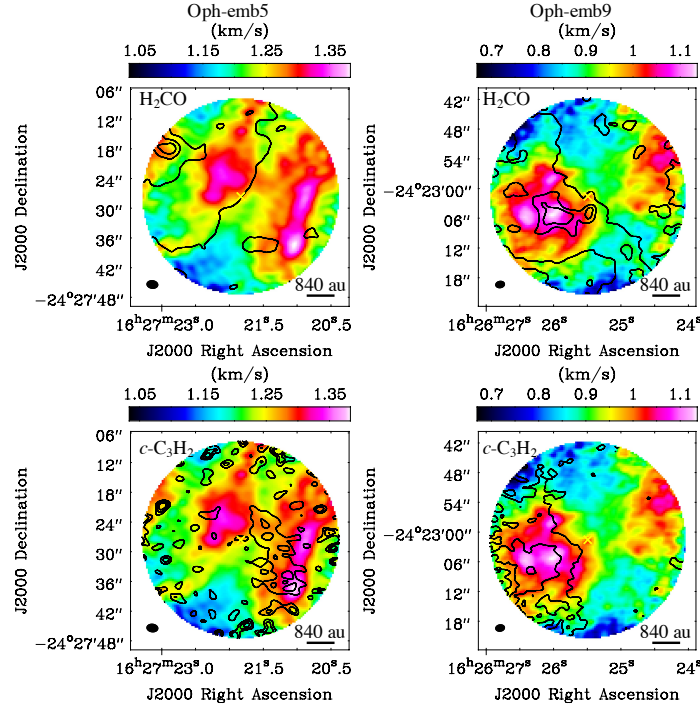


**Figure 10.** Moment 2 maps of the  $^{13}\text{CO}$  ( $J = 2 - 1$ ) line (color scales) overlaid by black contours showing moment 0 maps of the  $\text{H}_2\text{CO}$  ( $3_{0,3} - 2_{0,2}$ ) line (upper panels) and  $c\text{-C}_3\text{H}_2$  ( $6_{0,6} - 5_{1,5}$ ) line (bottom panels), respectively. Left and right panels show results in Oph-emb5 and Oph-emb9, respectively. The contour levels of the moment 0 images are the same as Figures 3 and 4. The yellow crosses indicate positions of the infrared sources (Enoch et al. 2009). The filled black ellipses indicate the angular resolutions of  $2''.2 \times 1''.5$  and  $1''.8 \times 1''.3$  for Oph-emb5 and Oph-emb9, respectively.

*Facilities:* Atacama Large Millimeter/submillimeter Array (ALMA)

*Software:* Common Astronomy Software Applications package (CASA; McMullin et al. 2007), CASSIS (Caux et al. 2011)

## APPENDIX

### A. CHANNEL MAPS OF $^{13}\text{CO}$ AND $\text{C}^{18}\text{O}$ LINES

Figures 11–14 show channel maps of the  $^{13}\text{CO}$  and  $\text{C}^{18}\text{O}$  lines towards Oph-emb5 and Oph-emb9, respectively.

## REFERENCES

- Adams, F. C. 2010, *ARA&A*, 48, 47.  
doi:10.1146/annurev-astro-081309-130830
- Adams, N. G. & Smith, D. 1985, *ApJL*, 294, L63.  
doi:10.1086/184510
- Artur de la Villarmois, E., Jørgensen, J. K., Kristensen, L. E., et al. 2019, *A&A*, 626, A71.  
doi:10.1051/0004-6361/201834877
- Bontemps, S., André, P., Kaas, A. A., et al. 2001, *A&A*, 372, 173. doi:10.1051/0004-6361:20010474
- Bouvier, J. & Appenzeller, I. 1992, *A&AS*, 92, 481
- Caselli, P. & Ceccarelli, C. 2012, *A&A Rv*, 20, 56.  
doi:10.1007/s00159-012-0056-x
- Caux, E., Bottinelli, S., Vastel, C., et al. 2011, *The Molecular Universe*, 280, 120
- Ceccarelli, C., Caselli, P., Fontani, F., et al. 2017, *ApJ*, 850, 176. doi:10.3847/1538-4357/aa961d
- Ceccarelli, C., Caselli, P., Bockelée-Morvan, D., et al. 2014, *Protostars and Planets VI*, 859.  
doi:10.2458/azu\_uapress.9780816531240-ch037
- Dunham, M. M., Allen, L. E., Evans, N. J., et al. 2015, *ApJS*, 220, 11. doi:10.1088/0067-0049/220/1/11
- Enoch, M. L., Evans, N. J., Sargent, A. I., et al. 2009, *ApJ*, 692, 973. doi:10.1088/0004-637X/692/2/973
- Esplugues, G., Cazaux, S., Caselli, P., et al. 2019, *MNRAS*, 486, 1853. doi:10.1093/mnras/stz1009

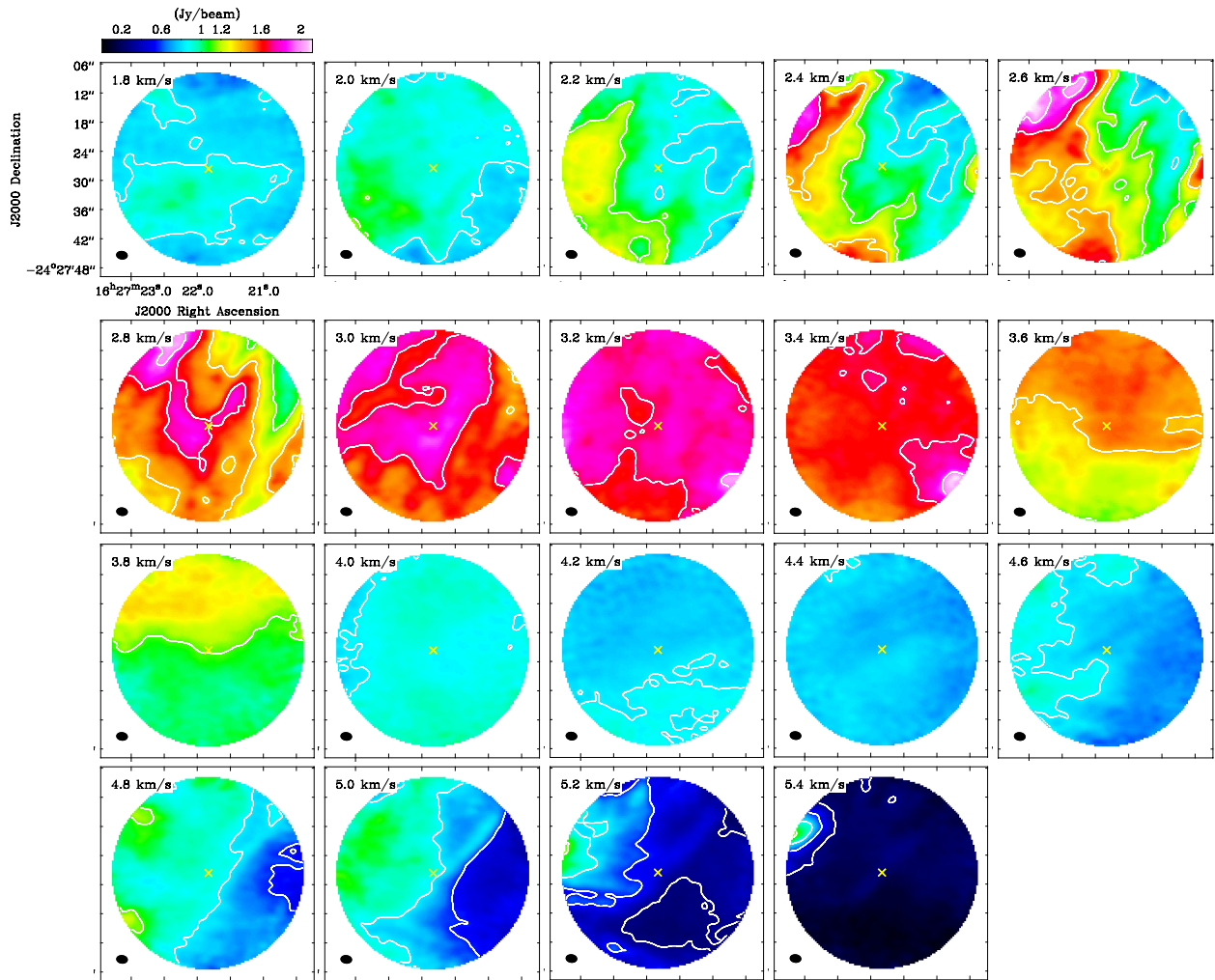


**Figure 11.** Channel maps of  $^{13}\text{CO}$  ( $J = 2 - 1$ ) toward Oph-emb5. Contour levels are in steps of  $50\sigma$  from  $50\sigma$  to  $350\sigma$  ( $1\sigma = 4.5 \text{ mJy beam}^{-1}$ ). The yellow crosses indicate positions of the infrared sources (Enoch et al. 2009). The filled black ellipses indicate the beam sizes of  $2''.2 \times 1''.5$ .

- Evans, N., Calvet, N., Cieza, L., et al. 2009, arXiv:0901.1691
- Hassel, G. E., Herbst, E., & Garrod, R. T. 2008, *ApJ*, 681, 1385. doi:10.1086/588185
- Herbst, E. & van Dishoeck, E. F. 2009, *ARA&A*, 47, 427. doi:10.1146/annurev-astro-082708-101654
- Jensen, S. S., Jørgensen, J. K., Kristensen, L. E., et al. 2019, *A&A*, 631, A25. doi:10.1051/0004-6361/201936012
- Kamazaki, T., Nakamura, F., Kawabe, R., et al. 2019, *ApJ*, 871, 86. doi:10.3847/1538-4357/aaf857
- Le Gal, R., Herbst, E., Dufour, G., et al. 2017, *A&A*, 605, A88. doi:10.1051/0004-6361/201730980
- Lindberg, J. E., Charnley, S. B., & Cordiner, M. A. 2016, *ApJL*, 833, L14. doi:10.3847/2041-8213/833/1/L14
- Lindberg, J. E., Charnley, S. B., Jørgensen, J. K., et al. 2017, *ApJ*, 835, 3. doi:10.3847/1538-4357/835/1/3
- Maluendes, S. A., McLean, A. D., & Herbst, E. 1993, *ApJ*, 417, 181. doi:10.1086/173301
- McMullin, J. P., Waters, B., Schiebel, D., et al. 2007, *Astronomical Data Analysis Software and Systems XVI*, 376, 127
- Millar, T. J., Bennett, A., & Herbst, E. 1989, *ApJ*, 340, 906. doi:10.1086/167444
- Müller, H. S. P., Schlöder, F., Stutzki, J., et al. 2005, *Journal of Molecular Structure*, 742, 215. doi:10.1016/j.molstruc.2005.01.027
- Murillo, N. M., van Dishoeck, E. F., van der Wiel, M. H. D., et al. 2018, *A&A*, 617, A120. doi:10.1051/0004-6361/201731724
- Öberg, K. I. & Bergin, E. A. 2021, *PhR*, 893, 1. doi:10.1016/j.physrep.2020.09.004
- Ortiz-León, G. N., Loinard, L., Dzib, S. A., et al. 2018, *ApJL*, 869, L33. doi:10.3847/2041-8213/aaf6ad



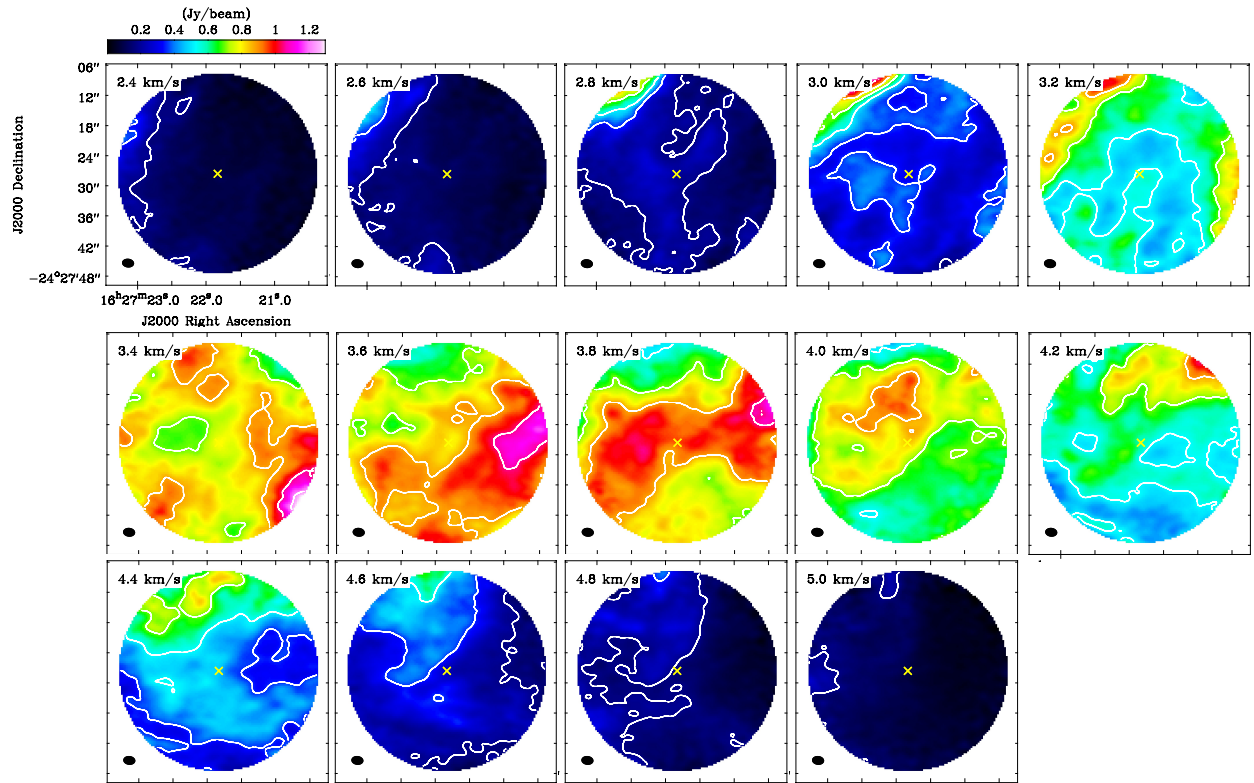


**Figure 12.** Channel maps of  $\text{C}^{18}\text{O}$  ( $J = 2 - 1$ ) toward Oph-emb5. Contour levels are in steps of  $50\sigma$  from  $50\sigma$  to  $350\sigma$  ( $1\sigma = 3.0$  mJy beam $^{-1}$ ). The yellow crosses indicate positions of the infrared sources (Enoch et al. 2009). The filled black ellipses indicate the beam sizes of  $2''.2 \times 1''.5$ .

Sakai, N., Sakai, T., Hirota, T., et al. 2008, *ApJ*, 672, 371.  
doi:10.1086/523635

Spezzano, S., Caselli, P., Pineda, J. E., et al. 2020, *A&A*, 643, A60. doi:10.1051/0004-6361/201936598

Spezzano, S., Gupta, H., Brünken, S., et al. 2016, *A&A*, 586, A110. doi:10.1051/0004-6361/201527460

Taniguchi, K., Herbst, E., Caselli, P., et al. 2019a, *ApJ*, 881, 57. doi:10.3847/1538-4357/ab2d9e

Taniguchi, K., Herbst, E., Majumdar, L., et al. 2021a, *ApJ*, 908, 100. doi:10.3847/1538-4357/abd6c9

Taniguchi, K., Majumdar, L., Takakuwa, S., et al. 2021b, *ApJ*, 910, 141. doi:10.3847/1538-4357/abe854

Taniguchi, K., Plunkett, A., Herbst, E., et al. 2020, *MNRAS*, 493, 2395. doi:10.1093/mnras/staa012

Taniguchi, K., Saito, M., Majumdar, L., et al. 2018, *ApJ*, 866, 150. doi:10.3847/1538-4357/aade97

Taniguchi, K., Saito, M., Sridharan, T. K., et al. 2019b, *ApJ*, 872, 154. doi:10.3847/1538-4357/ab001e

Tiwari, M., Menten, K. M., Wyrowski, F., et al. 2019, *A&A*, 626, A28. doi:10.1051/0004-6361/201834567

Turner, B. E. 2001, *ApJS*, 136, 579. doi:10.1086/322536

Vastel, C., Bottinelli, S., Caux, E., et al. 2015, SF2A-2015: Proceedings of the Annual meeting of the French Society of Astronomy and Astrophysics, 313

White, G. J., Drabek-Maunder, E., Rosolowsky, E., et al. 2015, *MNRAS*, 447, 1996. doi:10.1093/mnras/stu2323

Wiling, B. A., Meyer, M. R., Robinson, J. G., et al. 2005, *AJ*, 130, 1733. doi:10.1086/432758

Wright, E. L., Eisenhardt, P. R. M., Mainzer, A. K., et al. 2010, *AJ*, 140, 1868. doi:10.1088/0004-6256/140/6/1868

Yamagishi, M., Hara, C., Kawabe, R., et al. 2019, *ApJ*, 875, 62. doi:10.3847/1538-4357/ab0d80

Zhen, J., Castellanos, P., Paardekooper, D. M., et al. 2014, *ApJL*, 797, L30. doi:10.1088/2041-8205/797/2/L30

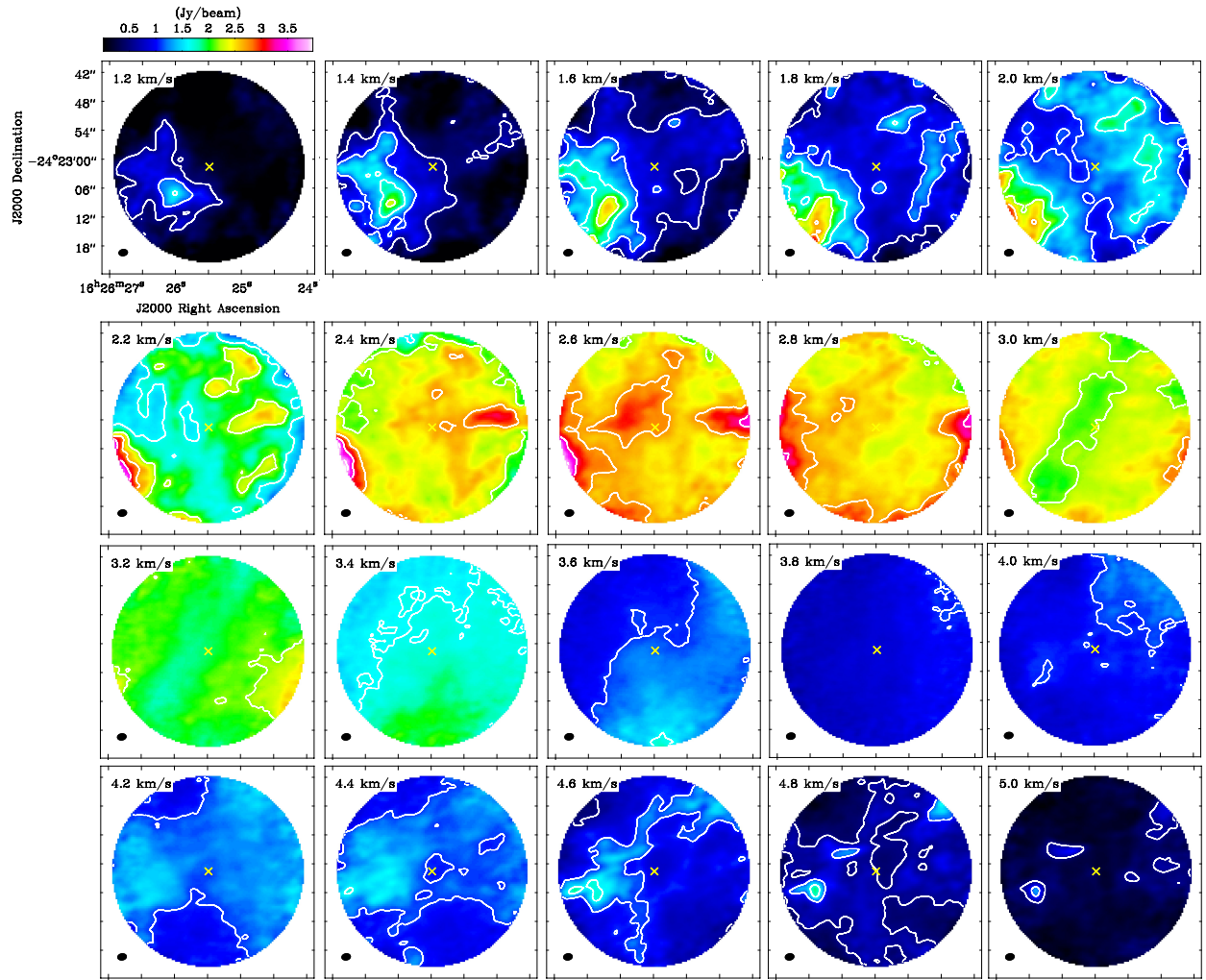


**Figure 13.** Channel maps of  $^{13}\text{CO}$  ( $J = 2 - 1$ ) toward Oph-emb9. Contour levels are in steps  $50\sigma$  from  $50\sigma$  to  $350\sigma$  ( $1\sigma = 10 \text{ mJy beam}^{-1}$ ). The yellow crosses indicate positions of the infrared sources (Enoch et al. 2009). The filled black ellipses indicate the beam sizes of  $1''.8 \times 1''.3$ .

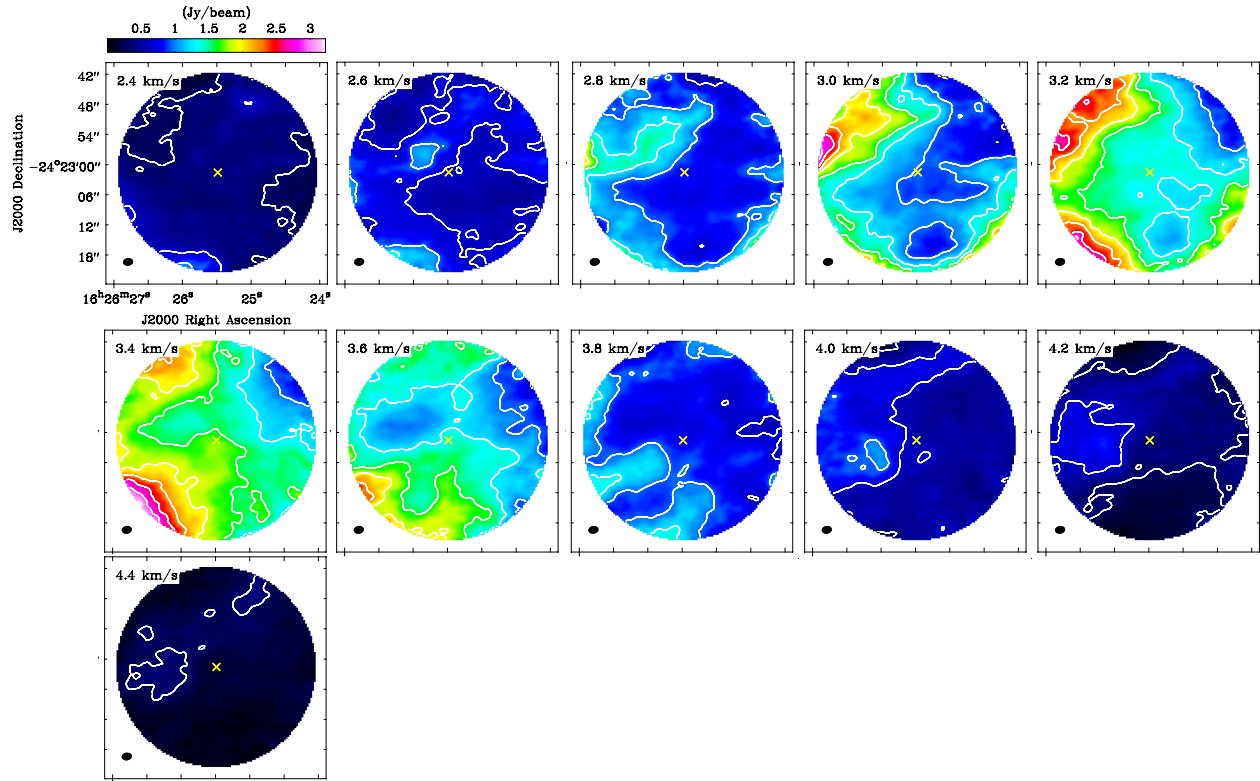


**Figure 14.** Channel maps of  $\text{C}^{18}\text{O}$  ( $J = 2 - 1$ ) toward Oph-emb9. Contour levels are in steps  $50\sigma$  from  $50\sigma$  to  $450\sigma$  ( $1\sigma = 6.7 \text{ mJy beam}^{-1}$ ). The yellow crosses indicate positions of the infrared sources (Enoch et al. 2009). The filled black ellipses indicate the beam sizes of  $1''.8 \times 1''.3$ .